Acta Crystallographica Section A
Foundations of Crystallography
ISSN 0108-7673

Received 7 November 2005
Accepted 3 April 2006

Extended dynamical HAADF STEM image simulation using the Bloch-wave method

Takashi Yamazaki,[a]* Kazuto Watanabe,[b] Koji Kuramochi[a] and Iwao Hashimoto[a]

[a]Department of Physics, Tokyo University of Science, Tokyo, 162-8601, Japan, and [b]Tokyo Metropolitan College of Industrial Technology, Tokyo, 140-0011, Japan. Correspondence e-mail: yamazaki@rs.kagu.tus.ac.jp

An extended method is proposed for the precise simulation of high-angle annular dark-field (HAADF) scanning transmission electron-microscope (STEM) images for materials containing elements with large atomic numbers and for thick specimens. The approach combines a previously reported method utilizing two kinds of optical potential [Watanabe, Yamazaki, Hashimoto & Shiojiri (2001). *Phys. Rev. B*, **64**, 115432] with a representation of a crystal sliced into multiple layers. The validity of the method is demonstrated by simulated images for elements with the diamond structure (Si, Ge and α-Sn) and for the perovskite $BaTiO_3$.

© 2006 International Union of Crystallography
Printed in Great Britain – all rights reserved

1. Introduction

Since the late 1980's (Pennycook & Boatner, 1988), high-angle annular dark-field scanning transmission electron-microscope (HAADF STEM) images have been used to analyze atomic structures (Pennycook & Nellist, 1999; Mcgibbon *et al.*, 1995; Chisholm *et al.*, 1998; Mitsuishi *et al.*, 1999; Yamazaki *et al.*, 2000). It is well known that each bright spot in a HAADF STEM image corresponds to the position of a column of atoms, and that the intensity of a spot depends on the atomic number of the element comprising the column except under certain defocus conditions (Watanabe, Yamazaki, Kikuchi *et al.*, 2001; Yamazaki *et al.*, 2001). Furthermore, the absence of the Fresnel interference effect and the high sensitivity of this technique to tilting of the crystal allow the precise determination of atomic structure at interfacial regions; for example, the interface of amorphous SiO_2 with crystalline Si has been studied at atomic resolution (Nakanishi *et al.*, 2004). However, computer simulations based on a dynamical theorem are indispensable for the precise quantitative analysis of HAADF STEM images.

There are two established methods for the dynamical simulation of these images: the multislice method (Kirkland *et al.*, 1987; Anderson *et al.*, 1997; Ishizuka, 2002) and the Bloch-wave method. The simulation approach, based on the Bloch-wave method for HAADF STEM images that are caused by incoherent thermal diffuse scattering (TDS), was first developed by Pennycook & Jesson (1990). This method was later extended to include images caused by coherent Bragg scattering (Nellist & Pennycook, 1999). Recently, Allen and co-workers (Allen, Findlay, Lupini *et al.*, 2003; Allen, Findlay, Oxley & Rossouw, 2003; Findlay *et al.*, 2003) simulated HAADF STEM images as well as electron energy-loss spectroscopy STEM images and energy-dispersive X-ray spectroscopy images by calculating the cross section for inelastic scattering. Watanabe and co-workers (Watanabe, Yamazaki, Hashimoto & Shiojiri, 2001; Watanabe, Kikuchi *et al.*, 2004) developed a different scheme based on the Bloch-wave method for the simulation of a variety of bright-field STEM, middle-angle annular dark field STEM and HAADF STEM images, taking into account both coherent Bragg scattering and TDS. Furthermore, the computing time and memory required were drastically decreased by including Bloch-wave symmetry and by performing the block diagonalization of a dispersion matrix (Watanabe, Asano *et al.*, 2004). The computing time needed for the simulation of a STEM image was reduced to 1/70 of that required using the standard Bloch-wave calculation.

The scheme proposed by Watanabe, Yamazaki, Hashimoto & Shiojiri (2001) uses two kinds of optical potentials to describe the TDS. The first potential quantifies the absorption due to TDS over all scattering angles. The second optical potential represents the absorption due to TDS outside the annular detector; this is a virtual potential. The channeling Bloch wave calculated using this virtual potential is also a virtual wavefunction. It gives rise to errors in the calculation of HAADF STEM images that are particularly serious for materials containing elements with large atomic numbers and for very thick specimens.

In this paper, the scheme proposed by Watanabe, Yamazaki, Hashimoto & Shiojiri (2001) is extended using the layer-by-layer representation described in §2. Simulated through-thickness HAADF STEM images for a variety of materials are shown in §3.

2. Theory

In order to reduce the errors that arise from the virtual optical potential, we divided a crystal into n layers as shown in Fig. 1. Using this layer-by-layer representation, the column vectors of

the Bloch-wave function in the ith layer at each partial incident wave can be defined by using the entrance $[z = t(i-1)/n = t_{i-1}]$ and exit $[z = ti/n = t_i]$ boundary conditions at the ith layer:

$$\Psi^{(i)}_{\rm all(ex)}(\mathbf{K}_\parallel, t_i) = \tilde{\mathbf{M}}^{(i)}_{\rm all(ex)}(\mathbf{K}_\parallel, t_i - t_{i-1}) \cdot \tilde{\mathbf{M}}^{(i-1)}_{\rm all}(\mathbf{K}_\parallel, t_{i-1} - t_{i-2}) \cdot \ldots \cdot \tilde{\mathbf{M}}^{(1)}_{\rm all}(\mathbf{K}_\parallel, t_1 - 0) \cdot \bar{\mathbf{U}}, \qquad (1)$$

where

$$\tilde{\mathbf{M}}^{(i)}_{\rm all(ex)}(\mathbf{K}_\parallel, t_i) = \exp(ik_z^{(i)} t_i)\tilde{\mathbf{C}}^{(i)}_{\rm all(ex)}(\mathbf{K}_\parallel) \cdot \tilde{\mathbf{\Gamma}}^{(i)}_{\rm all(ex)}(\mathbf{K}_\parallel, t_i) \cdot [\tilde{\mathbf{C}}^{(i)}_{\rm all(ex)}(\mathbf{K}_\parallel)]^{-1},$$

$\tilde{\mathbf{C}}^{(i)}_{\rm all(ex)}(\mathbf{K}_\parallel)$ is the matrix of eigenvectors, the matrix element $[\tilde{\mathbf{\Gamma}}^{(i)}_{\rm all(ex)}(\mathbf{K}_\parallel, t_i)]_{i,j} = \exp[i\gamma^{(j)}(\mathbf{K}_\parallel)]\delta_{i,j}$, $\gamma^{(j)}(\mathbf{K}_\parallel)$ is the conventional *Anpassung* for branch j and $\bar{\mathbf{U}}$ is a unit vector. The subscripts 'all' and 'ex' refer to calculations involving the optical potential due to TDS over all scattering angles and for scattering angles outside the detector, respectively; both calculations are only performed at the ith layer. All matrices except for the ith layer matrix in equation (1) are calculated using the TDS absorption over all scattering angles because it is necessary to describe the exact wavefunction as far as the $(i-1)$th layer in order to precisely calculate the difference in intensity at the ith layer. In the perfect crystal, the eigenvalues and eigenvectors are equal at the respective layers, so that superscripts are deleted from $\tilde{\mathbf{C}}$ and $\tilde{\mathbf{\Gamma}}$. In this case, equation (1) can be rewritten as

$$\Psi^{(i)}_{\rm all(ex)}(\mathbf{K}_\parallel, t_i) = \tilde{\mathbf{M}}_{\rm all(ex)}(\mathbf{K}_\parallel, t_i - t_{i-1}) \cdot \tilde{\mathbf{M}}_{\rm all}(\mathbf{K}_\parallel, t_{i-1}) \cdot \bar{\mathbf{U}}. \qquad (2)$$

Therefore, the convergent Bloch-wave functions (Hillyard & Silcox, 1995) are expressed by

$$\Phi^{(i)}_{\rm all(ex)}(\mathbf{K}_\parallel, \mathbf{R}, t_i, \mathbf{R}_0) = \int A(\mathbf{K}_\parallel) \sum_g [\Psi^{(i)}_{\rm all(ex)}(\mathbf{K}_\parallel, t_i)]_g \exp[i(\mathbf{K}_\parallel + \mathbf{g}) \cdot \mathbf{R}] \times \exp(-i\mathbf{K}_\parallel \cdot \mathbf{R}_0) \exp[-iW(\mathbf{K}_\parallel)]\, {\rm d}\mathbf{K}_\parallel, \qquad (3)$$

where $\mathbf{g}$ are the indices of the reciprocal-lattice waves, $A(\mathbf{K}_\parallel)$ is the aperture function, $\mathbf{R}_0$ is the position of the incident beam and $W(\mathbf{K}_\parallel)$ is the lens aberration function. The total intensities of the transmitted electrons at the ith layer, $I^{(i)}_{\rm all(ex)}(\mathbf{R}_0, t_i)$, are calculated from equation (3). Using the kinematical approximation for inelastic scattering, the HAADF STEM image formed by TDS is obtained by summing the absorption intensities in each layer:

$$I_{\rm TDS}(\mathbf{R}_0, t) = \sum_{i=1}^{n} [I^{(i)}_{\rm ex}(\mathbf{R}_0, t_i) - I^{(i)}_{\rm all}(\mathbf{R}_0, t_i)]. \qquad (4)$$

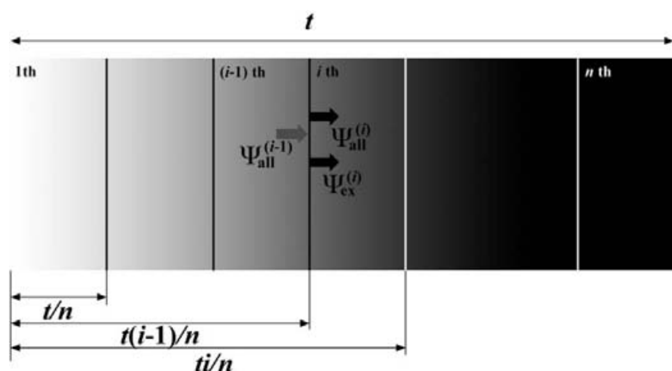

Figure 1
Schematic drawing of the layer structure of a perfect crystal.

3. Results and discussion

3.1. Simple substances

Simulated through-thicknesses of HAADF STEM images for [011]-orientated Si are shown in Figs. 2(*a*)–(*c*). In these simulations, the accelerating voltage was 200 keV, the semi-angle of the incident beam was 12.5 mrad, the spherical aberration was 1.0 mm, the defocus value was −50 nm (Scherzer defocus) and the detector range was 70–130 mrad. Under these conditions, the number of partial incident beams was 181, of which 25 were in the irreducible area. The excited wavefields in the crystal were calculated using 225 zero-order Laue-zone (ZOLZ) reflections and no high-order Laue-zone (HOLZ) reflections. These conditions are sufficient to describe the incident probe function onto the specimen and the exact Bloch wave into the crystal.

The images shown in Figs. 2(*a*)–(*c*) were simulated using a sample divided into $n = 1$, 4 and 8 slices, respectively. Through-thickness images were calculated by fixing the number of slices and increasing the thickness of each slice. Fig. 2(*a*) is thus the

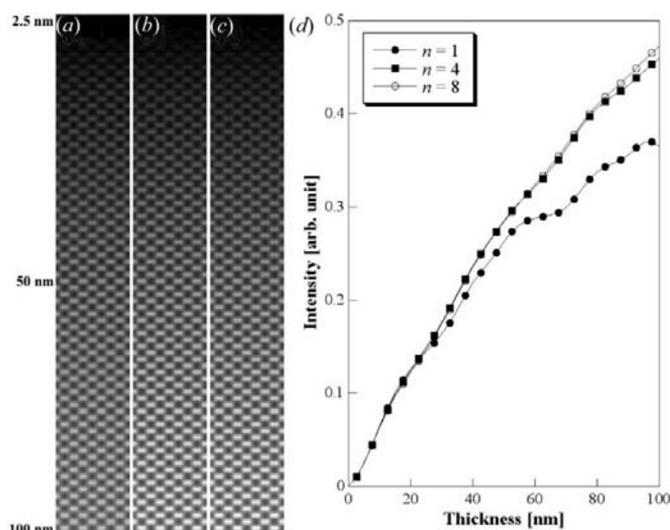

Figure 2
(*a*)–(*c*) Through-thicknesses of simulated HAADF STEM images for [011]-orientated Si where the sample is sliced into 1, 4 and 8 layers, respectively. The interval of the thickness series is 2.5 nm and the simulated area is 1 × 4 unit cells at each thickness. In these and all following image simulations, the same intensity scale relative to the incident electron beam is used in the calculations; zero electron intensity is shown as black and the maximum intensity for each figure is shown as white. (*d*) The maximum intensities at the positions of the atomic columns as a function of thickness.

image calculated by the original method (Watanabe, Yamazaki, Hashimoto & Shiojiri, 2001). It should be noted that the contrast is essentially unaffected by the number of slices. The maximum intensities at the positions of the atomic columns are plotted as a function of thickness in Fig. 2(*d*). It is apparent on comparing the maximum intensities that errors in the simulation appear for thicknesses greater than 60 nm in the case of $n = 1$. In contrast, the plots for $n = 4$ and 8 are almost identical for thicknesses between 0 and 100 nm. It is found that the errors resulting from the virtual optical potential can be ignored for specimens with more than four layers. In other words, it is necessary to set the slice thickness to less than 25 nm.

The intensity of a HAADF STEM image strongly depends on the atomic number of the element comprising the atomic column (Pennycook & Nellist, 1999). Therefore, HAADF STEM images can be exploited to analyze materials that contain high atomic number elements (Kawasaki *et al.*, 2001; Abe *et al.*, 2003). However, the errors in calculated images may be larger for heavy elements due to the virtual optical potential. We investigated this potential problem by performing simulations of Ge and α-Sn, which have the same diamond structure as Si. Figs. 3(*a*)–(*e*) show simulated through-thickness images for [011]-orientated Ge divided into n = 1, 4, 8, 12 and 16 slices, respectively. The amount of contrast in the images changes dramatically with the number of layers used; the dependence of the maximum intensities on the number of layers is shown in Fig. 3(*f*). Since a HAADF STEM image is proportional to the integration over specimen thickness of the product of the incoherent TDS cross section with the intensity of the convergent Bloch-wave field (Pennycook & Jesson, 1991; Pennycook & Nellist, 1999; Yamazaki *et al.*, 2000), the intensities of the spots may gradually increase with thickness. Although the results

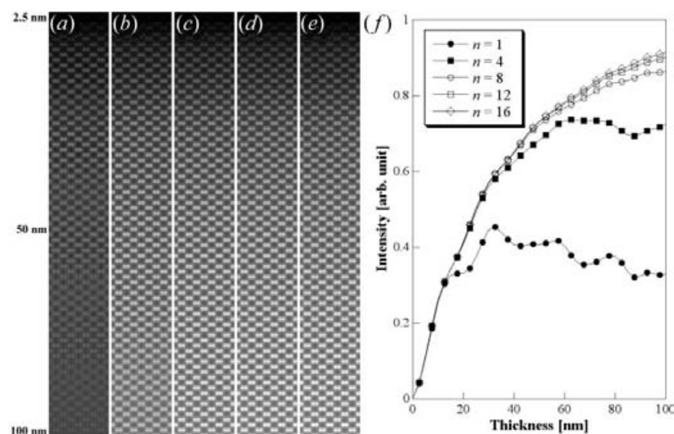

Figure 3
(*a*)–(*e*) Through-thicknesses of simulated HAADF STEM images for [011]-orientated Ge where the sample is sliced into 1, 4, 8, 12 and 16 layers, respectively. (*f*) The maximum intensities at the positions of atomic columns as a function of thickness.

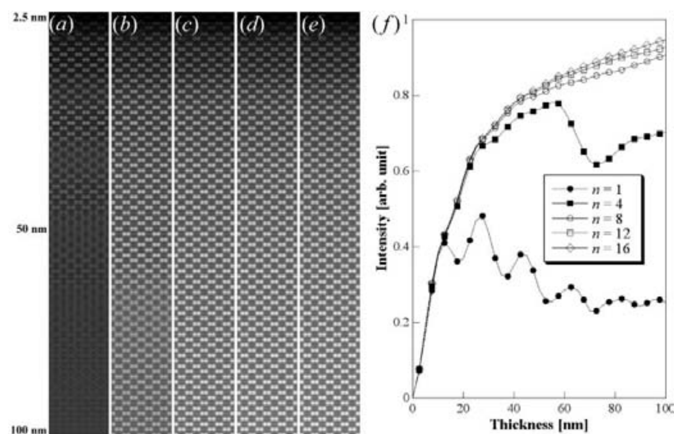

Figure 4
(*a*)–(*e*) Through-thicknesses of simulated HAADF STEM images for [011]-orientated α-Sn where the sample is sliced into 1, 4, 8, 12 and 16 layers, respectively. (*f*) The maximum intensities at the positions of atomic columns as a function of thickness.

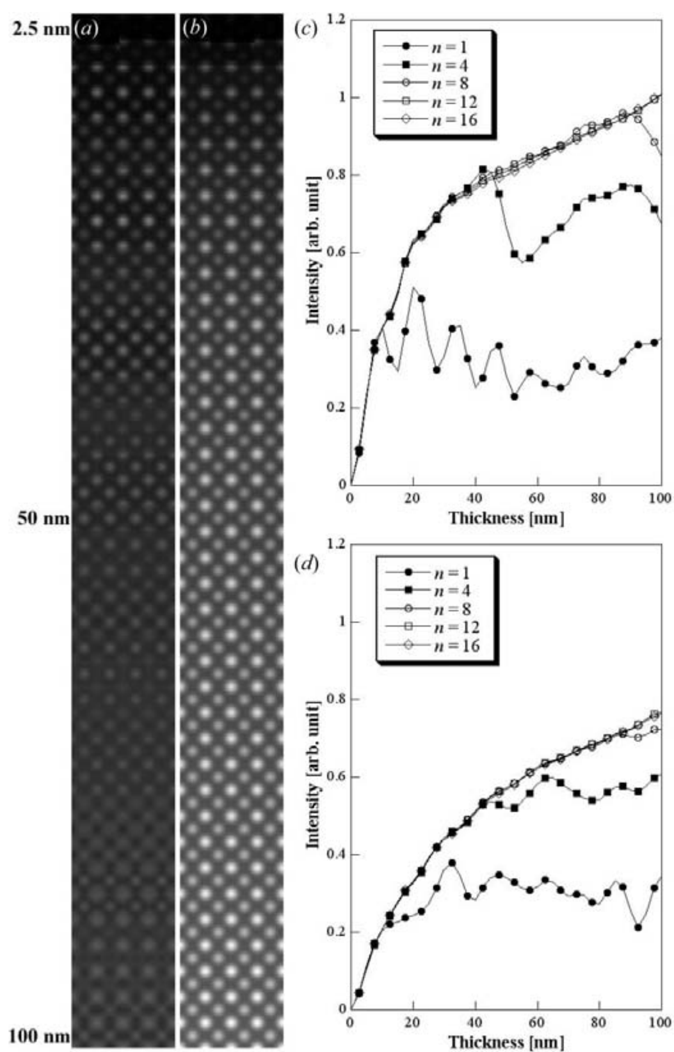

Figure 5
(*a*), (*b*) Through-thicknesses of simulated HAADF STEM images for [011]-orientated $BaTiO_3$, where the sample is sliced into 1 and 16 layers, respectively. (*c*), (*d*) The maximum intensities at the positions of Ba and Ti(O) columns as a function of thickness.

converge at a slice thickness of 25 nm in the case of Si, it is necessary to set the thickness to less than 12.5 nm for Ge.

Figs. 4(*a*)–(*e*) show the simulated through-thickness images for [011]-orientated α-Sn divided into n = 1, 4, 8, 12 and 16 slices, and the maximum intensities as a function of thickness are shown in Fig. 4(*f*). Within the present range of thickness, there is little difference between the results for Ge and α-Sn.

3.2. Compound materials

The simulation of HAADF STEM images for [001]-orientated orthorhombic $BaTiO_3$ was also performed. $BaTiO_3$ adopts the perovskite structure and the lattice constants used in the calculations were $a = b = 0.399$ and $c = 0.404$ nm. For this specimen, the number of partial incident waves was 201, of which 18 were inside the irreducible area. The dynamical simulation of $BaTiO_3$ used 251 ZOLZ reflections and no HOLZ reflections. The results converged for greater than 180 ZOLZ reflections. Figs. 5(*a*) and 5(*b*) display the through-thicknesses for simulated HAADF STEM images of specimens divided into n = 1 and 16 slices, respectively. The maximum intensities at the positions of Ba and Ti(O) columns are plotted as a function of thickness in Figs. 5(*c*) and 5(*d*), respectively. Fluctuations of the intensity with thickness are apparent for n = 1 and the bright-spot contrast does not depend on atomic number. Conversely, for the n = 16 specimen, neither the contrast nor the ratio of intensities between the Ba and Ti(O) columns depends on thickness. The intensities of both the Ba and Ti(O) columns converge to the same values when more than 8 layers are used.

4. Summary

We have proposed an extended scheme for the calculation of HAADF STEM images that is accurate for both materials comprised of elements with high atomic numbers and thick specimens. This is achieved by combining the layer-by-layer representation with the method utilizing two kinds of optical potential. The validity of our technique has been demonstrated by the simulation of images for Si, Ge and α-Sn with the diamond structure and for $BaTiO_3$ with the perovskite structure. This method is independent of atomic number and thickness and can be applied to any material without restriction.

This research was partially supported by the Kazato Research Foundation. This research was partially supported by the Ministry of Education, Science, Sports and Culture, Grant-in-Aid for Scientific Research (C), 15560024, 2003.

References

Abe, E., Pennycook, S. J. & Tsai, A. P. (2003). *Nature (London)*, **421**, 347–350.
Allen, L. J., Findlay, S. D., Lupini, A. R., Oxley, M. P. & Pennycook, S. J. (2003). *Phys. Rev. Lett.* **91**, 105503-1–4.
Allen, L. J., Findlay, S. D., Oxley, M. P. & Rossouw, C. J. (2003). *Ultramicroscopy*, **96**, 47–63.
Anderson, S. C., Birkeland, C. R., Antist, G. R. & Cockayne, D. J. H. (1997). *Ultramicroscopy*, **69**, 83–103.
Chisholm, M. F., Maiti, A., Pennycook, S. J. & Pantelides, S. T. (1998). *Phys. Rev. Lett.* **81**, 132–135.
Findlay, S. D., Allen, L. J., Oxley, M. P. & Rossouw, C. J. (2003). *Ultramicroscopy*, **96**, 65–81.
Hillyard, S. & Silcox, J. (1995). *Ultramicroscopy*, **58**, 6–17.
Ishizuka, K. (2002). *Ultramicroscopy*, **90**, 71.
Kawasaki, M., Yamazaki, T., Sato, S., Watanabe, K. & Shiojiri, M. (2001). *Philos. Mag. A*, **81**, 245–260.
Kirkland, E. J., Loane, R. F. & Silcox, J. (1987). *Ultramicroscopy*, **23**, 77–96.
Mcgibbon, A. J., Pennycook, S. J. & Angelo, J. E. (1995). *Science*, **269**, 518–521.
Mitsuishi, K., Kawasaki, M., Takeguchi, M. & Furuya, K. (1999). *Phys. Rev. Lett.* **82**, 3082–3084.
Nakanishi, N., Kikuchi, Y., Yamazaki, T., Okunishi, E., Watanabe, K. & Hashimoto, I. (2004). *Phys. Rev. B*, **70**, 165324-1–5.
Nellist, P. D. & Pennycook, S. J. (1999). *Ultramicroscopy*, **78**, 111–124.
Pennycook, S. J. & Boatner, L. A. (1988). *Nature (London)*, **336**, 565–567.
Pennycook, S. J. & Jesson, D. E. (1990). *Phys. Rev. Lett.* **64**, 938–941.
Pennycook, S. J. & Jesson, D. E. (1991). *Ultramicroscopy*, **37**, 14–38.
Pennycook, S. J. & Nellist, P. D. (1999). *Impact of Electron and Scanning Probe Microscopy on Material Research.* Dordrecht: Kluwer.
Watanabe, K., Asano, E., Yamazaki, T., Kikuchi, Y. & Hashimoto, I. (2004). *Ultramicroscopy*, **102**, 13–21.
Watanabe, K., Kikuchi, Y., Yamazaki, T., Asano, E., Nakanishi, N., Kotaka, Y., Okunishi, E. & Hashimoto, I. (2004). *Acta Cryst.* A**60**, 591–597.
Watanabe, K., Yamazaki, T., Hashimoto, I. & Shiojiri, M. (2001). *Phys. Rev. B*, **64**, 115432-1–5.
Watanabe, K., Yamazaki, T., Kikuchi, Y., Kotaka, Y., Kawasaki, M., Hashimoto, I. & Shiojiri, M. (2001). *Phys. Rev. B*, **63**, 085316-1–5.
Yamazaki, T., Kawasaki, M., Watanabe, K., Hashimoto, I. & Shiojiri, M. (2001). *J. Electron Microsc.* **50**, 517–521.
Yamazaki, T., Watanabe, K., Kikuchi, Y., Kawasaki, M., Hashimoto, I. & Shiojiri, M. (2000). *Phys. Rev. B*, **61**, 13833–13839.